

# SERF: Fine-Grained Interactive 3D Segmentation and Editing with Radiance Fields

Kaichen Zhou<sup>1</sup> Lanqing Hong<sup>2</sup> Enze Xie<sup>2</sup> Yongxin Yang<sup>2</sup> Zhenguo Li<sup>2</sup> Wei Zhang<sup>2</sup>  
<sup>1</sup>Peking University <sup>2</sup>Huawei Noah's Ark Lab

## Abstract

Although significant progress has been made in the field of 2D-based interactive editing, fine-grained 3D-based interactive editing remains relatively unexplored. This limitation can be attributed to two main challenges: the lack of an efficient 3D representation robust to different modifications and the absence of an effective 3D interactive segmentation method. In this paper, we introduce a novel fine-grained interactive 3D segmentation and editing algorithm with radiance fields, which we refer to as SERF. Our method entails creating a neural mesh representation by integrating multi-view algorithms with pre-trained 2D models. Building upon this representation, we introduce a novel surface rendering technique that preserves local information and is robust to deformation. Moreover, this representation forms the basis for achieving accurate and interactive 3D segmentation without requiring 3D supervision. Harnessing this representation facilitates a range of interactive 3D editing operations, encompassing tasks such as interactive geometry editing and texture painting. Extensive experiments and visualization examples of editing on both real and synthetic data demonstrate the superiority of our method on representation quality and editing ability.

## 1. Introduction

Recent advancements in neural rendering, exemplified by methods such as NeRF [38], MVSNeRF [8], and MiP-NeRF 360 [4], have significantly improved the accuracy of 3D shape reconstruction using 2D multi-view images. These developments have catalyzed the emergence of new 3D editing techniques, expanding the scope of interactive digital content manipulation. Despite this progress, current 3D editing methods confront substantial limitations, particularly in achieving fine-grained interaction and precise editing in 3D space. This gap is primarily due to the absence of an efficient 3D representation and a lack of effective 3D interactive segmentation methods, hindering the full exploitation of neural rendering's potential in 3D interactive editing.

Existing works in 3D editing, such as Neumesh [12] and

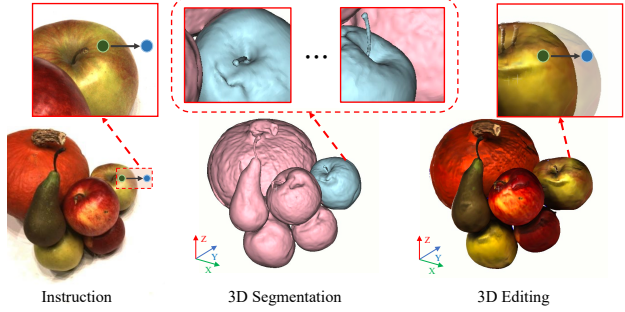


Figure 1. **3D Editing with SERF.** Our method achieves high-quality interactive 3D segmentation and editing.

Yuan et al. [71], require extensive training periods and depend on external software for editing functionalities. This dependence significantly increases the complexity and reduces the accessibility of 3D editing processes. Meanwhile, methods like ARF [72], Chiang et al. [11], Chen et al. [10], Huang et al. [23], and Fan et al. [14] focus mainly on global 3D style editing. These methods depend on supervision from pretrained 2D models, limiting their application to broader, less precise editing tasks. In contrast, approaches like Get3D [17] and SINE [3] offer direct editing in the feature space, deviating from the high-resolution 2D feature maps common in 2D editing. However, the coarser resolution of 3D feature volumes poses significant challenges for detailed, fine-grained 3D editing. Additionally, certain techniques, such as those exemplified by SEAL [62], require prior knowledge of an object's 3D position, confining their use to predefined 3D spaces and limiting the potential for spontaneous or creative modifications. Thus, achieving fine-grained 3D editing remains a significant challenge.

In this paper, we introduce a novel algorithm named SERF for interactive 3D segmentation and editing guided by 2D instructions (as illustrated in Figures 2 and 3). Our method initially employs established multi-view 3D reconstruction algorithms to construct a 3D mesh representation. We then augment this representation by incorporating 2D features from trained models, enhancing the accuracy and completeness of the information it encapsulates. Furthermore, our approach introduces a novel surface rendering process that preserves local information and demonstrates

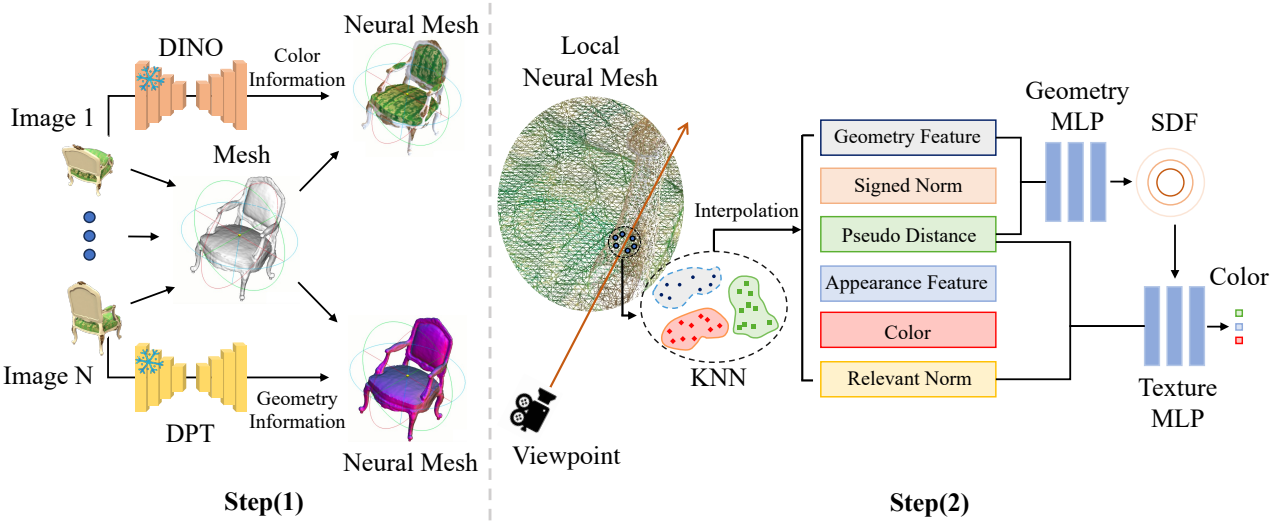


Figure 2. **Illustration of Mesh Construction and Surface Rendering in SERF.** The SERF involves 2 steps. In Step (1), a multi-view approach is employed to reconstruct the mesh, followed by projecting the color and geometry features extracted by trained 2D models onto the mesh to create the neural representation. In Step (2), the queried point considers the features of neighboring points, and these interpolated features are fed into texture and geometry MLPs to predict the final SDF and color.

robustness to global modifications. This process uniquely leverages local information to separate the learning processes for geometry and texture distinctly. Moreover, we incorporate an efficient 3D segmentation technique that leverages interactive 2D instructions and a pre-trained 2D segmentation model, which facilitates accurate 3D segmentation based on user inputs and enhances the intuitiveness of the editing process.

The main contributions of our work are threefold:

- We achieve enhanced scene reconstruction by integrating 2D features into our 3D representation. We establish a surface rendering process that preserves local information and demonstrates robustness to global modifications.
- Expanding on this representation, we present a novel 3D segmentation method that eliminates the need for fine-tuning when prompts are provided, relying solely on supervision from a 2D segmentation model.
- Based on the proposed methods, we demonstrate two types of editing operations: geometric editing, which allows for precise manipulation of geometry, and texture editing, which enables the modification of textures.

## 2. Related Works

**Novel View Synthesis.** Novel view synthesis aims to generate photo-realistic images from new viewpoints based on a set of posed image captures of a scene. Recent developments have integrated neural networks into the rendering process, leveraging various representations such as voxels [35, 53], point clouds [1, 13], multi-plane images (MPIs) [30, 36, 76], and implicit representations [39, 54]. A significant breakthrough in this area is the Neural Radiance Field (NeRF) [39], which uses a Multilayer Per-

ceptron (MLP) to encode scenes into a volumetric field. NeRF, with its volume rendering technique, has achieved outstanding results, including view-dependent effects, and has inspired a wide range of applications such as human rendering [43, 63], pose estimation [32], surface reconstruction [60, 67], and indoor scene rendering [70]. Further advancements and accelerations in NeRF’s MLP representation have been made using hybrid representations like voxels [50, 56], hashgrids [40], and tensorial decomposition [9, 57]. Despite these advancements, existing works in novel view synthesis often face challenges in fine-grained 3D editing due to limitations in representation accuracy and the complexity of integrating view synthesis with interactive 3D editing techniques.

**NeRF Segmentation.** The advent of NeRF in 3D novel view synthesis has catalyzed research in 3D segmentation within NeRF frameworks. A key development is Semantic-NeRF by Zhi *et al.* [74], which integrates semantic information into NeRFs’ appearance and geometry modeling, showcasing their potential in label propagation and refinement. Additionally, NVOS [47] introduces an interactive technique for selecting 3D objects in NeRFs using a specialized MLP trained with 3D features. There are also methods like N3F [58], DFF [27], LERF [25], and ISRF [18] that focus on converting 2D visual features to the 3D domain by training additional feature fields. Further, various instance and semantic segmentation approaches [5, 15, 16, 21, 34, 42, 52, 55, 59, 69] have been integrated with NeRFs, broadening the capabilities of NeRF segmentation. However, these methods often require significant modifications or retraining of NeRF models and

involve intricate feature-matching processes, posing challenges in practical and efficient 3D editing applications.

**3D Editing.** The realm of scene editing in computer vision and graphics has seen substantial evolution, transitioning from single-view editing techniques, such as insertion [29, 77], relighting [31], composition [44], and object movement [26, 51], to more complex neural rendering-based approaches. These advanced methods encompass scene-level, object-level, and pixel-level editing. Scene-level editing includes altering global attributes like lighting [19] and color palettes [28], while intrinsic decomposition methods [20, 22, 41, 68, 73, 78] enable more detailed modifications. At the object level, techniques such as Object-NeRF [65] and Liu *et al.* [33] facilitate manipulation within neural radiance fields, though they are primarily restricted to rigid transformations. NeuMesh [12] marks a stride in pixel-level editing with its fine-grained control, yet it is constrained by the limitations of mesh scaffolds. Despite these advancements, a major drawback in the field remains the optimization for efficiency, with many methods requiring extensive optimization and inference times for practical editing applications.

### 3. Methodology

The user is provided with a set of multi-view images  $\{I_1, I_2, \dots, I_N\}$  that capture a 3D scenario from different viewpoints  $\{C_1, C_2, \dots, C_N\}$ . To initiate the editing process, the user begins by selecting a random image  $I_u$ . From there, the user can segment out the specific part they wish to edit using prompts **pr** and provide the editing instructions  $I_u^e$  for that segment. This allows the user to focus on a particular region of interest and provide targeted instructions for the desired modifications.

The goal of SERF is to generate a set of modified multi-view images  $\{I_1^e, I_2^e, \dots, I_N^e\}$  based on the edited image  $I_u^e$ . The primary objective is to ensure that the modified images remain consistent with the edited image  $I_u^e$ . This means that the modifications applied to  $I_u^e$  should be reflected consistently across all the generated multi-view images, resulting in a coherent set of modified images. To achieve this, this methodology is divided into four parts. Firstly, we utilize a previously developed multi-view geometry estimation algorithm to reconstruct the mesh representation  $M$  of the target 3D scenario. Using  $M$ , we combine the geometry and appearance features provided by trained 2D models to reconstruct the Neural Mesh Representation  $\bar{M}$ , as described in Section 3.1. Secondly, based on the Neural Mesh  $\bar{M}$ , we employ a previously introduced volume rendering technique to establish the connection between  $\bar{M}$  and the set of multi-view images  $\{I_1, I_2, \dots, I_N\}$ . To facilitate the subsequent editing process, we separate the rendering process

into geometry and appearance learning, outlined in Section 3.1. Thirdly, in order to achieve accurate 3D editing, we generate a 3D segmented mesh  $M^s$  corresponding to the edited segmented image  $I_u^e$ , as explained in Section 3.3. Lastly, based on the proposed view synthesis model and 3D mesh segmentation model, we present two possible editing methods for demonstration purposes.

#### 3.1. Neural Mesh Construction

To obtain the Neural Mesh Representation  $\bar{M}$ , we start by using existing multi-view methods as NeuS [60] to reconstruct a 3D mesh representation  $M$  that consists of around 10,000 - 20,000 vertices. However, this initial mesh only provides coarse geometry information and lacks detailed features. Previous methods like NeuMesh [12] assigns optimizable features to each vertex. The optimization process involves computationally intensive tasks, including optimizing the networks that establish the connections between the mesh representation and the input images, as well as optimizing the assigned feature vectors.

In contrast, we propose a novel approach to enhance the generalizability and efficiency of our method. Instead of relying on an optimized process to calculate the final geometry and appearance feature vectors, we introduce a technique that aggregates features extracted by pre-trained 2D models onto the reconstructed mesh  $M$ . By leveraging pre-trained 2D models, we can extract rich and informative features from the input images.

We utilize the pre-trained unsupervised model DINO [6] to extract hierarchical appearance features corresponding to the images  $\{I_1, I_2, \dots, I_N\}$ . The DINO [6] model comprises a *conv*-layer followed by 12 *transformer* layers. From these layers, we extract feature maps from the 4<sup>th</sup>, 8<sup>th</sup>, and 12<sup>nd</sup> positions, which we use to construct the appearance feature map  $\{\mathcal{F}_n^a\}$  for frame  $I_n$ . Similarly, we employ the monocular depth estimation model DPT [45] to extract the geometry feature map  $\{\mathcal{F}_n^g\}$  for frame  $I_n$ .

Using the extracted appearance features  $\{\mathcal{F}_n^a\}$  and geometry features  $\{\mathcal{F}_n^g\}$ , our goal is to assign a feature vector to each vertex of the constructed mesh  $M$  in order to create the neural mesh representation  $\bar{M}$ . To achieve this, we follow the following steps: (1) Given a frame  $I_n$  and the camera matrix  $C_n$ , we estimate the corresponding depth  $D'_n$  based on the mesh  $M$ . This depth information is used to compute the corresponding 3D point  $P$  for each pixel  $p$  using the equation  $P = D'_n(p)K_nC_np$ , where  $K_n$  represents the intrinsic camera matrix and we assume that  $K_n$  is known. (2) The pixel-wise appearance feature  $\mathcal{F}_n^a(p)$  and geometry feature  $\mathcal{F}_n^g(p)$  can then be assigned to the 3D points  $P$  based on the aforementioned relationship. This assigns the corresponding features to each point in the mesh. (3) By reprojecting all the pixel-wise features into the 3D point space, we obtain a set of neural points  $\{\mathcal{P}_n\}_{n=1}^N$ ,

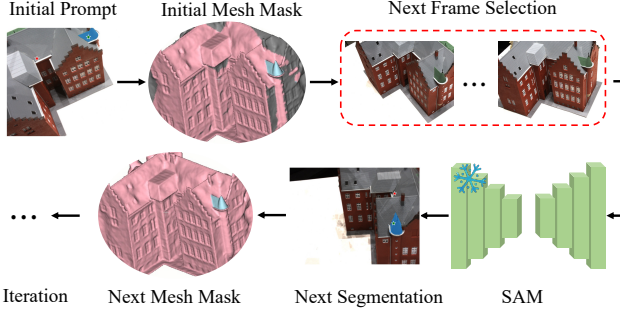


Figure 3. **Illustration of 3D Segmentation Pipeline.**

where  $\mathcal{P}_n$  represents the 3D points associated with frame  $I_n$ . (4) For each vertex  $V$  in the mesh  $M$ , we find the  $K$  closest points from the neural points obtained in the previous step. These closest points serve as the neighboring points for vertex  $V$ :

$$\{P_k\}_{k=1}^{k=K} = \operatorname{argmin}_K (V - P)^2. \quad (1)$$

By performing these steps, we can assign feature vectors to each vertex in the mesh, enabling the construction of the neural mesh representation  $\bar{M}$ . The feature of vertice  $V$  could be written as:

$$\mathcal{F}(V) = \sum_{k=1}^{k=K} w_k \mathcal{F}(P_k) / \sum_{k=1}^{k=K} w_k, \quad w_k = \frac{1}{\|P_k - V\|}, \quad (2)$$

where  $w_k$  is the weight based on the inversed distance.

### 3.2. Surface Rendering

**Rendering.** Based on the constructed Neural Mesh  $\bar{M}$ , our objective is to utilize surface rendering techniques to achieve accurate view synthesis. This view synthesis should possess two key characteristics. Firstly, it should be robust to the deformation of the neural mesh representation. Secondly, it should allow for texture editing without altering the geometric features.

To accomplish these goals, we introduce a rendering process that relies on locally relevant positions rather than global positions to predict corresponding information. Additionally, our learning process involves two components: geometry nets  $f_g(\cdot)$  and appearance net  $f_a(\cdot)$ . The geometry nets are responsible for predicting the local signed distance field  $s$  for a given queried point  $P$ . This can be expressed as follows:

$$s = f_g(n_s, \mathcal{F}_g(P), \hat{d}), \quad n_s = - \sum_{k=1}^{k=K} w_k (\mathbf{n}_P \cdot \mathbf{n}_{V_k}^T) / \sum_{k=1}^{k=K} w_k \quad (3)$$

In this equation,  $\mathcal{F}_g(P)$  represents the weighted geometry feature obtained by querying nearby vertices using an inverse process similar to Eqn. 2. The term  $\hat{d} = \sum_{k=1}^{k=K} w_k \|P - V_k\| / \sum_{k=1}^{k=K} w_k$  denotes the distance be-

tween the queried point and the surface hit point. Additionally,  $\mathbf{n}_s$  is utilized to approximate the angle-weighted normal vector, as proposed in the work [2]. Using the predicted SDF information, we can estimate the color information as follows:

$$c = \mathcal{F}_a(\mathbf{n}_r, \mathcal{F}_a(P), \nabla_P s, \hat{d}); \quad \mathbf{n}_r = \sum_{k=1}^{k=K} w_k (\mathbf{n}_P - \mathbf{n}_{V_k}^T) / \sum_{k=1}^{k=K} w_k \quad (4)$$

where  $f_g(P)$  is the weighted appearance feature by querying nearby vertices based on the inversed process of Eqn. 2;  $\nabla_P s$  is the gradient of predict SDF along the ray.

Please note that the positional encoding technique proposed in NeRF [38] is utilized to process normal vectors and distances. However, for the sake of brevity, we omit the detailed description of the positional encoding in this context. Following the formulation of NeuS and quadrature rules, we perform the rendering process for the pixel  $\hat{C}$  using a set of points. These points are specifically chosen based on the principles of NeuS and the quadrature rules, which ensure accurate and efficient rendering computations.

$$\hat{C} = \sum_{i=1}^N T_i \alpha_i \mathbf{c}_i, \quad T_i = \prod_{j=1}^{i-1} (1 - \alpha_j), \quad (5)$$

$$\alpha_j = \max \left( \frac{\Phi_s(s_i) - \Phi_s(s_{i+1})}{\Phi_s(s_i)}, 0 \right), \quad (6)$$

where  $T$  represents the accumulated transmittance;  $\Phi_s$  denotes the cumulative distribution of the logistic distribution; and  $\alpha$  represents the opacity derived from the adjacent Signed Distance Function (SDF).

**Loss Function.** To supervise the learning process, we utilize two loss functions: one for color information and one for density information. Following the approach of NeRF, the loss function for color information can be expressed as  $\mathcal{L}_c = \sum_{j \in J} \|\hat{C}(j) - C(j)\|_2^2$ . This loss function measures the discrepancy between the predicted color  $\hat{C}(j)$  and the ground truth color  $C(j)$  at each pixel  $j$ .

Similarly, the loss function for the signed distance field (SDF) information can be written as  $\mathcal{L}_s = \sum_{h \in H} \|\hat{s}(h) - s(h)\|_2^2$ . Here, the SDF loss function quantifies the difference between the predicted SDF  $\hat{s}(h)$  and the coarse SDF  $s(h)$ . To compute the SDF information, we rely on the reconstructed mesh  $M$  and employ the algorithm in [61].

Additionally, following a similar approach to NeuMesh, we incorporate an Eikonal loss to regularize the norm of the spatial gradients to 1. This loss term, denoted as  $\mathcal{L}_{re}$ , is formulated as  $\mathcal{L}_{re} = \sum_k \|\|\nabla_P s_P\| - 1\|_2^2$ . The Eikonal loss ensures that the spatial gradients of the signed distance field ( $s_P$ ) have a magnitude of 1, promoting smooth and consistent variations in the distance values across the surface.

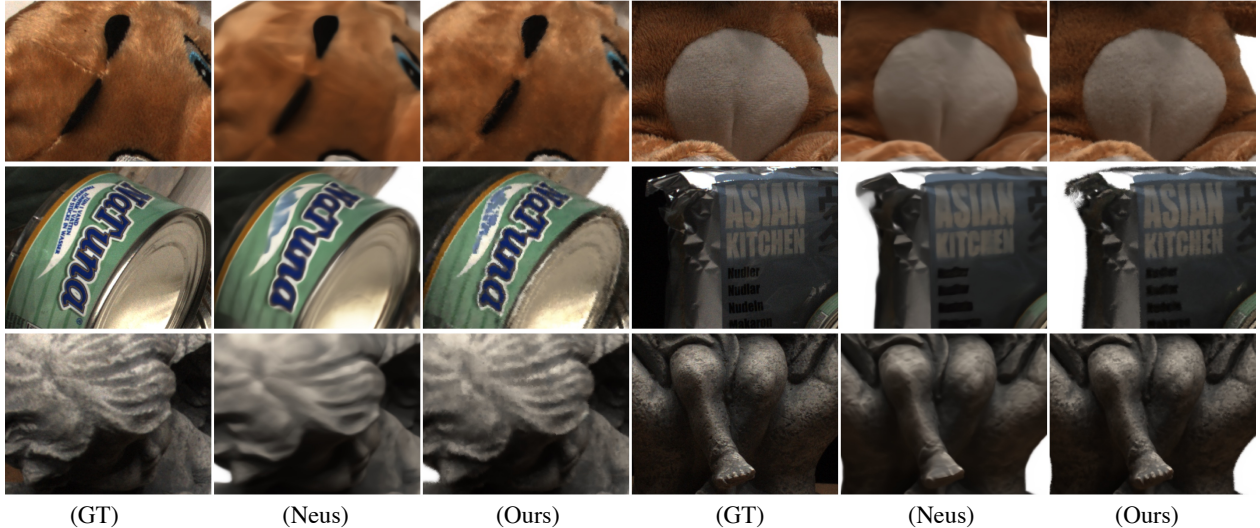


Figure 4. **Comparisons on DTU Scenes for Novel View Synthesis.** In comparison to the NeuS model, SERF demonstrates superior view synthesis results for both texture and geometry information reconstruction.

Methods	DTU			NeRF 360° Synthetic		
	PSNR $\uparrow$	SSIM $\uparrow$	LPIPS $\downarrow$	PSNR $\uparrow$	SSIM $\uparrow$	LPIPS $\downarrow$
NeuTex [64]	26.080	0.893	0.196	25.718	0.914	0.109
NeuS [60]	26.352	0.909	0.176	30.588	<b>0.960</b>	0.058
NeuMesh [12]	28.289	0.921	<b>0.117</b>	30.945	0.951	0.043
Ours	<b>29.113</b>	<b>0.924</b>	0.121	<b>31.701</b>	0.954	<b>0.037</b>

Table 1. **Quantitative Results for View Synthesis on DTU and NeRF Synthetic.** Our method achieves the best performance while enabling interactive segmentation and editing on both two datasets.

### 3.3. 3D Mesh Segmentation

In order to achieve precise 3D editing using the edited segmented frame  $I_u^e$ , we need to extend the 2D segment mask to a 3D representation. Having accurate 3D segmentation is crucial as it helps us identify the specific parts that require modification while keeping the remaining parts static. In contrast to 2D images, where methods like SAM (Segment Anything) offer efficient interactive segmentation solutions, there is no widely available interactive 3D segmentation technique. Although SAM3D [7] provides a possible solution, it is limited to handling large foreground objects and requires fine-tuning when prompts are updated. To address this challenge, in this section, we propose an efficient 3D scene segmentation approach based on 2D supervision. Our method mainly consists of the following steps.

- (a) The 2D mask  $\mathbf{m}_{pre} = p_j$ ,  $p_j \in \{0, 1\}$ , representing the mask of initial image  $I_{pre}$  provided by the user, is generated using prompts  $\mathbf{pr}_{pre}^{obj}$  for objects and  $\mathbf{pr}_{pre}^{oth}$  for the remaining parts, along with a trained SAM.
- (b) To generate a 3D masked vertices  $\mathcal{M} = V_j$ ,  $V_j \in \{-1, 0, 1\}$ , we back-project the 2D mask  $\mathbf{m}_{pre}$  into the 3D space. In this representation, the values  $-1$  indicate parts that do not appear in the  $\mathbf{m}_{pre}$  mask, the values  $0$  represent parts marked as "others", and the values  $1$  rep-

resent parts marked as "objects".

- (c) In this step, we aim to choose the most suitable next frame for masking. Given the vertex  $\mathcal{V} = V_j$ ,  $V_j \in \{0, 1\}$  corresponding to image  $I$ , where  $1$  denotes vertices viewed by image and  $0$  denote vertices wouldn't be viewed, the next frame is chosen as:

$$I_{new} = argmax(\mathcal{V} \cdot (\mathcal{M}')^T), \quad (7)$$

$$\mathcal{M}' = \mathcal{M}, \mathcal{M}'[V_j == -1] = 0. \quad (8)$$

- (e) With the new frame  $I_{new}$ , we aim to provide new prompts  $\mathbf{pr}_{new}^{obj}$  and  $\mathbf{pr}_{new}^{oth}$ . Here, we assume that the previously provided prompts are accurate and we want to generate new prompts as close as to all  $\mathbf{pr}_{pre}$  as possible. We first compute the corresponding vertices  $V_{pre}^{obj}$  of  $\mathbf{pr}_{pre}^{obj}$ . Thus the corresponding vertices  $V_{new}^{obj}$  could be written as:

$$V_{new}^{obj} = argmin(d), \quad (9)$$

$$d = \sum_{pre} ||\mathcal{V}[V_j == 1] - V_{pre}^{obj}||, \quad (10)$$

where  $d$  is the distance between each vertex and previous denoted prompts. A similar method is used to choose the  $V_{new}^{oth}$ . Both  $V_{new}^{oth}$  and  $V_{new}^{obj}$  are projected to 2D space to

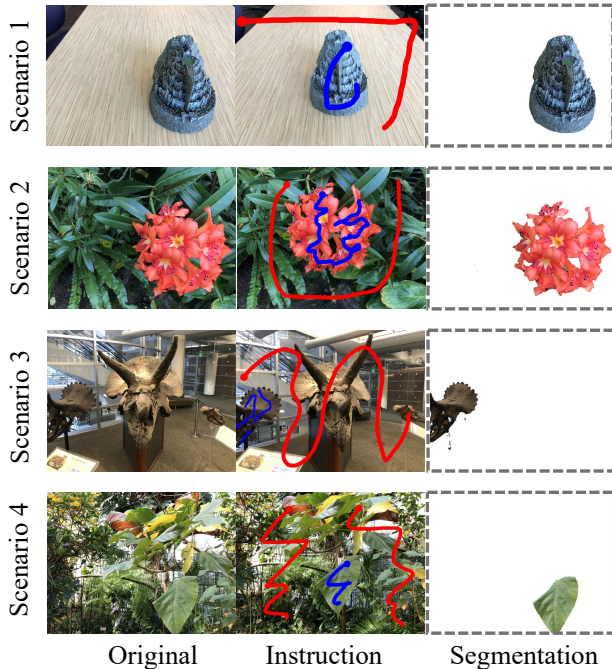


Figure 5. **Results of 3D Interactive Segmentation Using SERF.** The red lines represent content to be deleted, while the blue lines represent content to be preserved.

generate new pixel-wise prompts  $\mathbf{pr}_{new}^{oth}$  and  $\mathbf{pr}_{new}^{obj}$ . The new mask  $I_{new}^m$  is generated with the help of prompts and SAM. We set  $\mathbf{m}_{new} = \mathbf{m}_{pre}$  and restart from step (b).

It is worth mentioning that in step (b), when fusing the 2D mask  $\mathbf{m}_{pre}$  with the 3D mask  $\mathcal{M}$ , directly replacing all vertices in  $\mathcal{M}$  with the values provided by  $\mathbf{m}_{pre}$  could lead to abnormal segmentation results in a few frames. To address this issue, we employ a mitigation strategy. For each vertex  $V$ , we compare the segmentation results provided by all previous frames, denoted as  $\{\mathcal{M}_n\}_{n=1}^N$ . If in the majority of frames, vertex  $V$  is masked as 1 (indicating it belongs to the object), we classify it as an 'object'. Conversely, we classify it as 'others'. By adopting this approach, we take into account the consistency of segmentation across multiple frames, enabling more reliable and accurate segmentation results. This helps to mitigate the issue of abnormal segmentation and ensures a more robust and consistent segmentation process. Once the consistent 3D mask  $\mathcal{M}$  is generated, we can project it onto each frame to generate a corresponding mask for each frame. This projection process involves mapping the 3D mask onto the 2D image plane of each frame to obtain a frame-specific mask. By projecting the 3D mask onto each frame, we can accurately segment the object of interest in each individual frame, enabling further analysis and editing at the frame level.

### 3.4. 3D Editing

Building upon the previously proposed Neural Mesh Construction and 3D Mesh Segmentation methods, we will now

focus on implementing two specific types of editing. It's important to note that although we only present these two editing methods, our approach can be extended to other editing operations, such as scaling.

**Geometry Deformation.** Our representation is primarily based on an explicit mesh representation, which enables us to achieve consistent multi-view geometric editing by manipulating the 3D neural mesh. In order to maintain local consistency within the 3D representation, we have deviated from the traditional volume rendering process, which relies on global positions. Instead, we calculate local normals and relevant distances between queried points and vertices. This allows us to infer the structure and appearance information of the 3D scenario. Our Experiment section includes several examples that demonstrate these concepts.

In our proposed single-view-based 3D editing approach, we first utilize a 3D segmentation method to create a mask for vertices that are subject to deformation and vertices that are intended to remain static. Next, we employ a mesh deformation algorithm, such as ARAP (As-Rigid-As-Possible), to transform the shape of the 3D mesh. Finally, the 3D neural mesh is used to construct the 3D appearance information.

**Texture Painting.** In addition to 3D geometry deformation, we introduce texture painting operations for 3D editing. This allows users to draw directly on a selected frame  $I_r^e$  from the provided frames  $I_1, I_2, \dots, I_N$ . Instead of modifying the UV mapping, our approach, called SERF, offers a more intuitive way to perform texture painting.

To begin the texture painting process, we start with the edited frame  $I_r^e$ . First, we segment the edited region  $\mathbf{m}_e$  by comparing  $I_r^e$  with the corresponding original frame  $I_r$ . This segmentation helps identify the specific area that has been modified.

Next, we compute the feature  $\mathcal{F}_a$  of  $I_r^e$ , capturing the appearance information of the edited frame. We then back-project the 2D mask  $\mathbf{m}_e$  into 3D vertices, resulting in the vertex mask  $\mathcal{V}_m$ . This vertex mask indicates which vertices of the neural mesh  $\bar{\mathcal{M}}^e$  are affected by the edited region.

Using the vertex mask  $\mathcal{V}_m$ , we modify the appearance feature of the neural mesh  $\bar{\mathcal{M}}^e$  for the masked-out vertices. This ensures that the texture changes applied to the edited region are reflected in the 3D representation.

Finally, based on the edited mesh  $\bar{\mathcal{M}}^e$ , we fine-tune our appearance network for several minutes. This step helps refine the network to better capture the appearance changes introduced through the texture painting process.

By incorporating texture painting operations into our approach, we provide users with the ability to directly manipulate and enhance the visual details of 3D objects. This expands the range of editing possibilities and offers a more in-

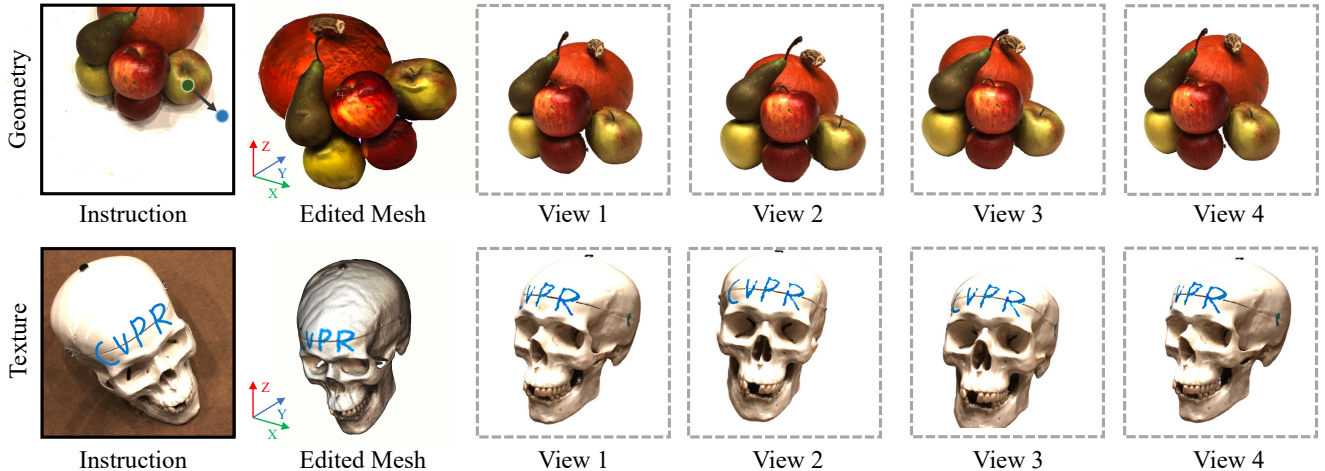


Figure 6. **Example of 3D Interactive Editing with SERF.** Our approach allows for interactive geometry editing (1st row) and interactive appearance editing with fine-tuning, a process that takes only a few minutes (2nd row).

Method	DTU Scan ID															Avg.
	24	37	40	55	63	65	69	83	97	105	106	110	114	118	122	
NeuTex [64]	2.078	5.038	3.477	1.039	3.744	2.078	3.201	2.163	5.104	1.828	1.951	4.319	1.177	3.100	1.921	2.815
NeuS [60]	1.544	1.224	1.065	0.665	1.286	0.825	0.904	1.350	1.320	0.855	0.987	1.328	0.487	0.636	0.678	1.010
NeuMesh [12]	1.112	1.262	0.988	0.674	1.224	0.835	<b>0.878</b>	1.232	1.304	0.741	0.963	1.239	0.558	0.645	0.739	0.960
Ours	<b>1.038</b>	<b>1.213</b>	<b>0.979</b>	<b>0.656</b>	<b>1.222</b>	<b>0.817</b>	0.898	<b>1.150</b>	<b>1.296</b>	<b>0.732</b>	<b>0.946</b>	<b>1.190</b>	<b>0.468</b>	<b>0.625</b>	<b>0.651</b>	<b>0.942</b>

Table 2. **Quantitative Results for Mesh Reconstruction on DTU.** We compare mesh quality using Chamfer distance on the DTU dataset. We use training split of images instead of full images, so the result of NeuS [60] is different from the original paper.

tuitive and natural way to modify textures without the need for complex UV mapping adjustments.

## 4. Experiments

To demonstrate the advantages of our method, we conduct a series of experiments aimed at providing comprehensive evidence of its capabilities in various aspects, including (1) novel view synthesis, (2) 3D mesh segmentation, and (3) 3D interactive editing. Detailed experimental settings and additional visualization results are provided in the Appendix.

**Datasets.** Our experiments are conducted on various datasets, including DTU [24], NeRF Synthetic [38], and NVOS [46]. For the DTU dataset [24], we used the IDR [66] configuration, utilizing 15 scenes with images of 1600 × 1200 resolution and accompanying foreground masks. To facilitate metric evaluation for both rendering and mesh quality, we randomly selected 10% of the images as a test split and used the remaining images for training. For the NeRF Synthetic dataset, we adhered to the official split guidelines. The NVOS dataset [46], derived from the LLFF dataset [37], features several forward-facing scenes. Each scene in NVOS includes a reference view with scribbles and a target view, accompanied by 2D segmentation masks.

## 4.1. View Synthesis

We first conduct an evaluation of view synthesis performance across several surface rendering techniques. We include comparisons with NeuTex [64], NeuS [60], and NeuMesh [12]. The experimental setup follows Xiang et al. [64], assessing each method on two benchmark datasets, i.e., DTU and NeRF 360° Synthetic with three metrics, namely PSNR, SSIM, and LPIPS. We also measure the mesh reconstruction quality with the Chamfer distances in the same way as Wang et al. [60].

**Results.** As shown in Table 1, our method demonstrates state-of-the-art (SOTA) performance in novel view synthesis on both the DTU and NeRF synthetic datasets. Specifically, our approach achieves the highest PSNR scores of 29.113 and 31.701 on the DTU and NeRF Synthetic datasets, respectively. Besides, as detailed in Table 2, our method consistently outperforms the baseline methods across most of the DTU Scan IDs regarding Chamfer distance. This demonstrates the superior accuracy of our method in reconstructing mesh details. Visualizations are provided in Figure 4. These results underscore the efficacy of our method in rendering high-quality views. Furthermore, our method facilitates interactive editing capabilities, adding a layer of practical utility.

Method	mIoU (%)	Acc (%)	Tuning
NVOS [47]	70.1	92.0	✓
SA3D [7]	<b>90.3</b>	<b>98.2</b>	✓
Graph-Cut (3D) [49]	39.4	73.6	
ISRF [18]	83.8	96.4	
Ours	<b>90.3</b>	97.6	

Table 3. Quantitative Results for 3D Segmentation on NVOS in terms of mIoU (Intersection-Over-Union) and Accuracy. Tuning refers to whether fine-tuning is necessary for the model when presented with new prompts.

Method	PSNR↑	SSIM↑	LPIPS↓
SERF (K=4)	30.487	0.944	0.060
SERF (w/o $n_s$ )	31.150	0.951	0.043
SERF (w/o $n_r$ )	31.413	0.952	0.041
SERF (K=8)	<b>31.701</b>	<b>0.954</b>	<b>0.037</b>

Table 4. Quantitative Results of Ablation Studies for SERF on NeRF Synthetic.

## 4.2. 3D Interactive Segmentation

In this section, we present the results of our study on 3D mesh segmentation, which is guided by interactive instructions. The objective is to demonstrate the effectiveness of our method in accurately segmenting reconstructed meshes based on user-provided 2D instructions. We conduct experiments involving SERF and three contemporary learning-based interactive segmentation techniques: NVOS [47], ISRF [18], and SA3D [7]. It is important to note that while NVOS and SA3D require network fine-tuning to adapt to new prompts, ISRF and our SERF are designed to be effective without such fine-tuning.

**Results.** As shown in Table 4, SERF achieves performance on par with SA3D, despite the latter’s reliance on fine-tuning to new prompts. Our method attains a mean Intersection over Union (mIoU) of **90.3%** and an accuracy of 97.6%, which are competitive with the best-performing method in our study. These results are significant as they highlight the efficiency of SERF in interactive segmentation tasks, offering comparable accuracy to fine-tuned models while eliminating the need for such adjustments. Figure 5 further illustrates our method’s segmentation results on the NVOS dataset, underscoring its practical application in mesh segmentation scenarios.

## 4.3. 3D Interactive Editing

**Interactive Geometry Editing.** In this section, we demonstrate the effectiveness of our method in interactive 3D geometry editing. As illustrated in Figure 6 (specifically in the first row), our approach enables users to manipulate an object within a view interactively. This manipulation directly alters the corresponding 3D mesh, leading to coherent and synchronized changes across different viewpoints. This experiment highlights our algorithm’s capability not only in

generating realistic and visually appealing views but also in maintaining the consistency of the reconstructed mesh during dynamic geometry modifications. Such interactive editing underscores the practical utility of our method in applications requiring real-time 3D scene manipulation and visualization.

**Interactive Appearance Editing.** We further demonstrate the capabilities of our method in interactive surface editing. Our approach enables users to modify an object’s surface within a view. For instance, as a part of our experiment, we alter the object’s surface by adding the text “CVPR” in one viewpoint, as illustrated in Figure 6 (in the second row). This modification is reflected in the corresponding mesh, leading to changes in the reconstructed views from new perspectives. The experiment showcases how our algorithm facilitates not only the modification of the mesh’s appearance but also ensures that these changes are consistently translated across different views. The result is visually compelling and customized outputs, illustrating the practical utility of our method in applications that require detailed and personalized surface editing.

## 4.4. Ablation Studies

To evaluate the performance of the proposed module, we conducted ablation studies by establishing several baseline scenarios. These include: SERF (K=4), which considers only 4 neighboring points as the baseline; SERF (w/o  $n_s$ ), representing the baseline but excluding the proposed pseudo signed normal vector; SERF (w/o  $n_r$ ), which uses the conventional direction of the corresponding ray instead of the proposed relevant normal vector; and SERF (K=8), representing the standard case. Our findings reveal that the absence of both  $n_s$  and  $n_r$  significantly reduces SERF’s performance, with the most notable decrease occurring when the number of neighboring points, K, is reduced.

## 5. Conclusion

In our study, we introduce SERF, an efficient algorithm for interactive 3D segmentation and editing without fine-tuning per user prompts by blending multi-view 3D reconstruction with advanced 2D techniques to create an efficient neural mesh representation. This approach facilitates precise 3D segmentation and interactive editing, enhancing scene reconstruction accuracy and offering innovative geometric and appearance editing capabilities. Through extensive experiments, SERF has shown superior performance in quality and editing ability across various datasets, representing a significant stride in 3D-based interactive editing and paving the way for future advancements in the field.

## 6. Appendix

### 6.1. Method

#### 6.1.1 Mesh Construction

A crucial aspect of our approach involves establishing a prior mesh prior to the training of the Appearance Net and Geometry Net. We use the following two pure RGB methods for generating the final mesh information.

**Mesh Construction Based On Multi-View Depth Estimation** Mesh reconstruction can be achieved through leveraging existing multi-view depth estimation (MDE) techniques such as MVSNet and Cascade MVSNet. One notable benefit of this approach is its generalizability, requiring only fine-tuning to adapt to new datasets.

For a set of images  $I_1, I_2, \dots, I_N$ , the task is to estimate the corresponding depth images  $D_1, D_2, \dots, D_N$ . However, to determine the depth  $D_n$  for image  $I_n$ , multi-view depth estimations (MDEs) necessitate two or more reference views. The simplest approach involves selecting the nearest views based on the distance between different viewpoints. Nonetheless, solely estimating the depth  $D_n$  for  $I_n$  results in sparse and noisy outcomes. Therefore, we propose the following steps to estimate  $D_n^1, D_n^2, \dots, D_n^W$  depth maps for image  $I_n$ :

- With camera poses denoted as  $C_1, C_2, \dots, C_N$ , the first step entails determining the nearest distance  $d$  between distinct camera poses. Following this, we apply a radius equal to  $3d$  in the ball-pivoting technique to construct the mesh structure derived from these camera poses.
- The camera set  $C^{t1}, C^{t2}, C^{t3}$  is formed by utilizing the three vertices of each triangle in the camera mesh structure. Specifically, we assign  $C^{t1}$ ,  $C^{t2}$ , and  $C^{t3}$  as the target frame, while the remaining two cameras function as reference frames. For each triangle, three depth maps— $D^{t1}, D^{t2}$ , and  $D^{t3}$ —are generated.
- However, utilizing  $D^{t1}, D^{t2}$ , and  $D^{t3}$  directly can lead to noisy results. Consequently, we propose a method to reduce the noise in the generated depth. To elucidate the denoising process, we take  $D^{t1}$  as an example. (1) We employ  $D^{t1}$  to project all points  $\mathcal{P}^{t1}$  in frame  $I^{t1}$  to frame  $I^{t2}$  as  $\mathcal{P}_{t2}^{t1}$  and to frame  $I^{t3}$  as  $\mathcal{P}_{t3}^{t1}$  with the assistance of extrinsic parameters  $R|T$  and the intrinsic matrix  $K$ . (2) We subsequently re-project  $\mathcal{P}_{t2}^{t1}$  and  $\mathcal{P}_{t3}^{t1}$  back to frame  $I^{t1}$ , resulting in  $\hat{\mathcal{P}}_{t2}^{t1}$  and  $\hat{\mathcal{P}}_{t3}^{t1}$ . (3) For each point  $P$ , we employ the following equation to assess its validity:

$$V(P) = (||\mathcal{P}^{t1}(P) - \hat{\mathcal{P}}_{t3}^{t1}(P)|| + ||\mathcal{P}^{t1}(P) - \hat{\mathcal{P}}_{t2}^{t1}(P)||) < \epsilon \quad (11)$$

where  $\epsilon$  is the threshold  $\epsilon$  to check the validation.

Upon generating a set of depth maps, the final point clouds  $\mathcal{P}$  can be derived. To construct the ultimate mesh  $M$ , we employ the Poisson surface reconstruction feature available in MeshLab, resulting in the final mesh as depicted in

Fig. (a).

#### Mesh Construction Based On Neural Radiance Field

While the multi-view depth estimation (MDE) method suggests a versatile approach to mesh construction, the resulting mesh may still exhibit noise. If fine-tuning is feasible, NeuS [60] is employed to reconstruct the corresponding mesh for each specific scenario. In the original NeRF, the computation of color information is as follows:

$$C(\mathbf{o}, d) = \int_0^{+\infty} w(t)c(P(t), d)dt, \quad (12)$$

where  $C(\mathbf{o}, d)$  is the output color for this pixel,  $w(t)$  a weight for the point  $P(t)$ . However, according the NeuS  $w(t)$ , the weight  $w(t)$  in Eqn. 12 attains a local maximum at a point before the ray reaches the surface point. Thus, the new weight function is construct as:

$$w(t) = \frac{\Phi_s(f(P(t)))}{\int_0^{+\infty} \Phi_s(f(P(u)))du}, \quad (13)$$

where  $\Phi_s$  is the cumulative distribution of the logistic distribution and  $f(\cdot)$  is the function to predict SDF information. The final mesh is shown in Fig. 7. Meshes generated from NeuS are used in our view synthesis process. The main problem of mesh generated by the MVSNet is that they couldn't provide an accurate normal map and smooth surface for the final map, which leads to longer training time.

#### 6.1.2 Interactive Editing

##### Geometry Editing

**Image-Based Instruction** As depicted in the main text, the process of geometry editing typically involves two sequential steps: initially, we isolate the deformed portion using the suggested interactive segmentation method, and subsequently, employing the point-based illustration, we apply the deformation algorithm to modify the existing mesh.

However, we've discovered that our algorithm not only supports the point-based illustration but also accommodates an image-based algorithm with the assistance of scene flow estimation. Specifically, once we obtain the edited image  $I_u^e$  for the frame  $I_u$ , we can first estimate the depth  $D_u$  using the constructed mesh  $M$  and the optic flow map  $\{e\}$  with the assistance of a pre-trained optic flow model—in our case, we utilize FlowFormer. Subsequently, we leverage  $D_u$  and  $\{e\}$  to estimate the scene flow  $\{f^e\}$  by applying the scene flow MLP proposed in DynPoint [75] and SINE [3]. Since we already have segmentation for dynamic points and static points, we can introduce an additional constraint to restrict the scene flow. To ensure the object's rigidity, only points in the dynamic part  $P_d$  will possess a scene flow value, while points in the static part  $P_s$  will not have a scene flow value.

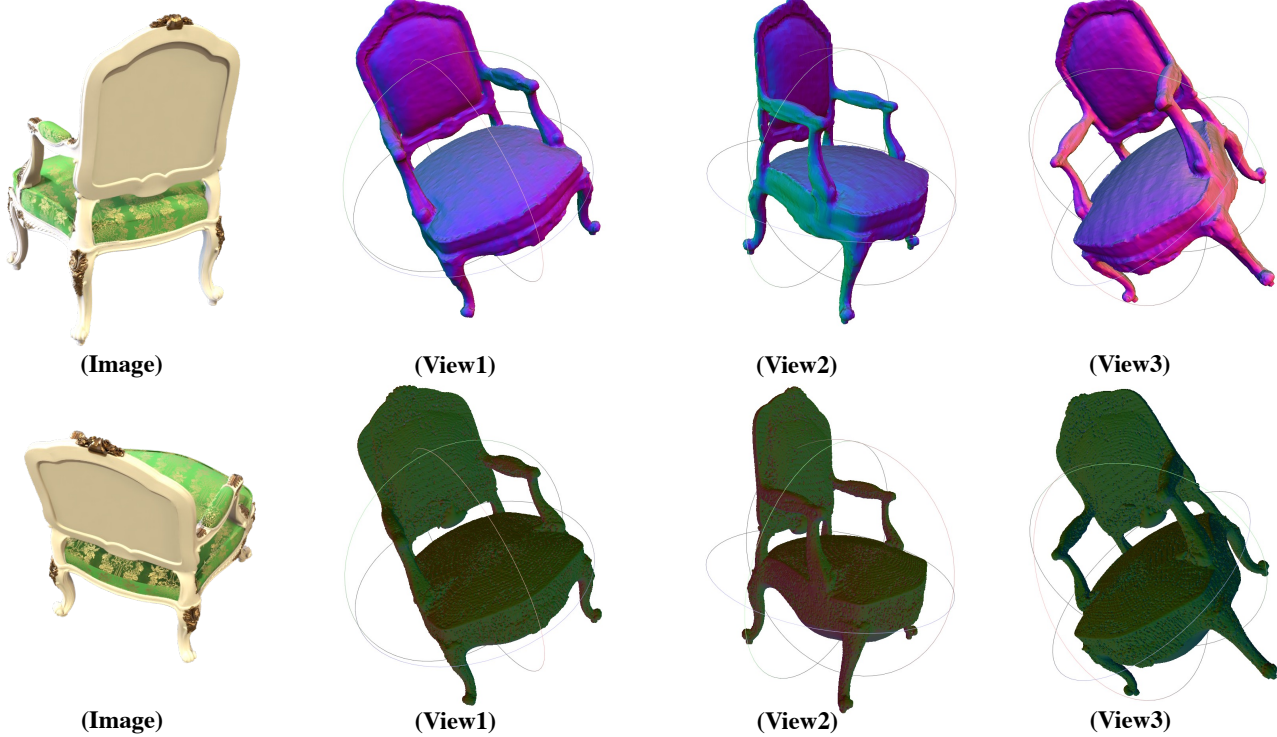


Figure 7. **Comparisons of Meshes Constructed By MVSNet and NeuS.** The top row is generated using NeuS, and the bottom row is generated using MVSNet. The color is determined by mapping the normal vectors to a scale that falls within the range of [0, 1].

### 6.1.3 Structure of Networks

To capture color features, we employ the SMALL Dino backbone with a patch size of 8. We extract outputs from the 4<sup>th</sup>, 8<sup>th</sup>, and 12<sup>th</sup> layers to create hierarchical feature maps. However, these feature maps are only 1/8 the size of the original input image, and the dimensionality change is too substantial for direct use in the final prediction. Therefore, prior to incorporating DINO hierarchical features into the neural mesh construction process, we apply an average pooling layer along the channel dimension of the feature map to reduce its channel dimensions. Subsequently, we utilize bilinear interpolation for both the height and width dimensions. It’s noteworthy that, given the utilization of a vision transformer as the encoder in the DPT model, we employ a similar technique to process the feature maps from the encoder.

The structure of our MLP modules is shown in Fig. 9.

## 6.2. Experiment

### 6.2.1 Evaluation Metrics

In this section, we outline the computational process for the evaluation metrics utilized in our experiments. They can be

expressed as follows:

$$\text{PSNR} = 10 \cdot \log_{10} \left( \frac{\text{MAX}^2}{\text{MSE}} \right), \quad (14)$$

where, MAX represents the maximum possible pixel value in the image, and MSE is the mean squared error between the original and reconstructed images.

$$\text{SSIM}(x, y) = \frac{(2\mu_x\mu_y + C_1)(2\sigma_{xy} + C_2)}{(\mu_x^2 + \mu_y^2 + C_1)(\sigma_x^2 + \sigma_y^2 + C_2)}, \quad (15)$$

where  $x, y$  are the original and reconstructed images;  $\mu$  and  $\sigma$  are the mean and the variances;  $C_1, C_2$  are constants to stabilize the division with weak denominator.

$$\text{LPIPS}(x, y) = \sum_i w_i \cdot d_i(x, y), \quad (16)$$

where,  $d_i(., .)$  represents the perceptual distance at scale  $i$  between original image and reconstructed image;  $w_i$  represents the weight associated with scale  $i$ .

$$IoU_i = \frac{\text{TP}_i}{\text{TP}_i + \text{FP}_i + \text{FN}_i}; \quad (17)$$

$$mIoU = \frac{1}{N} \sum_{i=1}^N IoU_i; \quad (18)$$

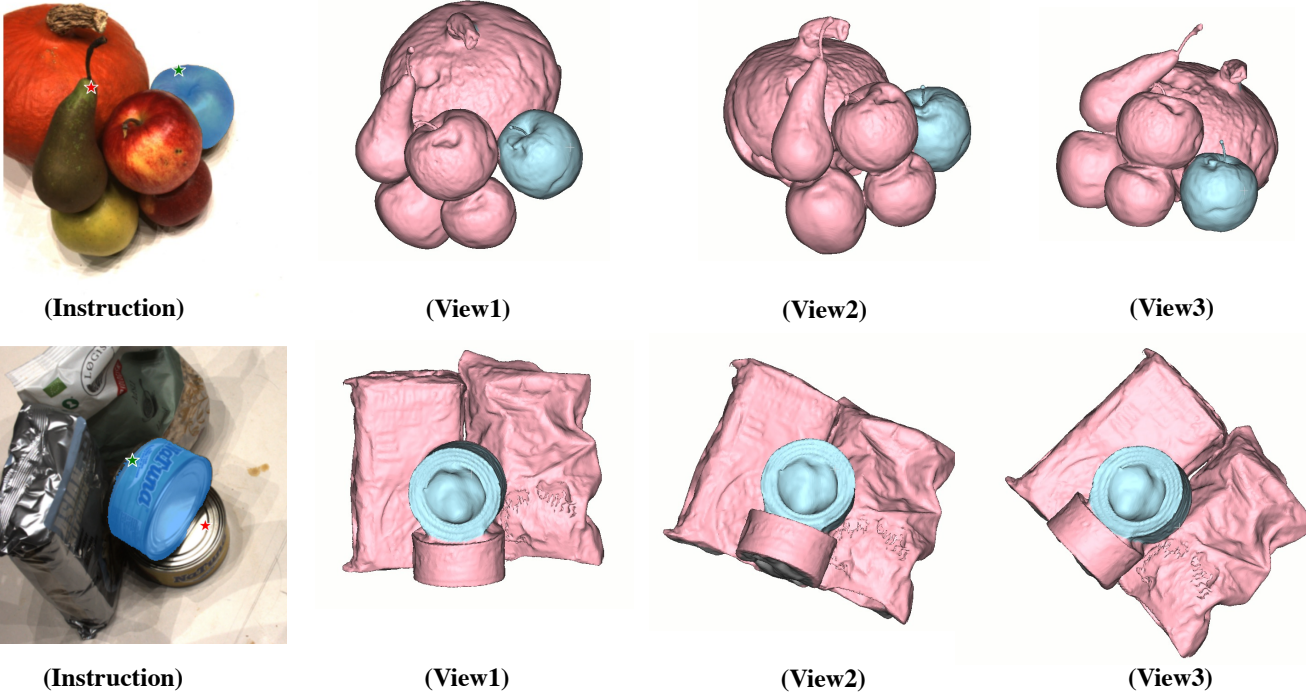


Figure 8. **More Qualitative Result of Interactive Segmentation.** The user’s instructions for a specific image are displayed in the left column, while the right columns depict the segmentation results generated by our algorithm.

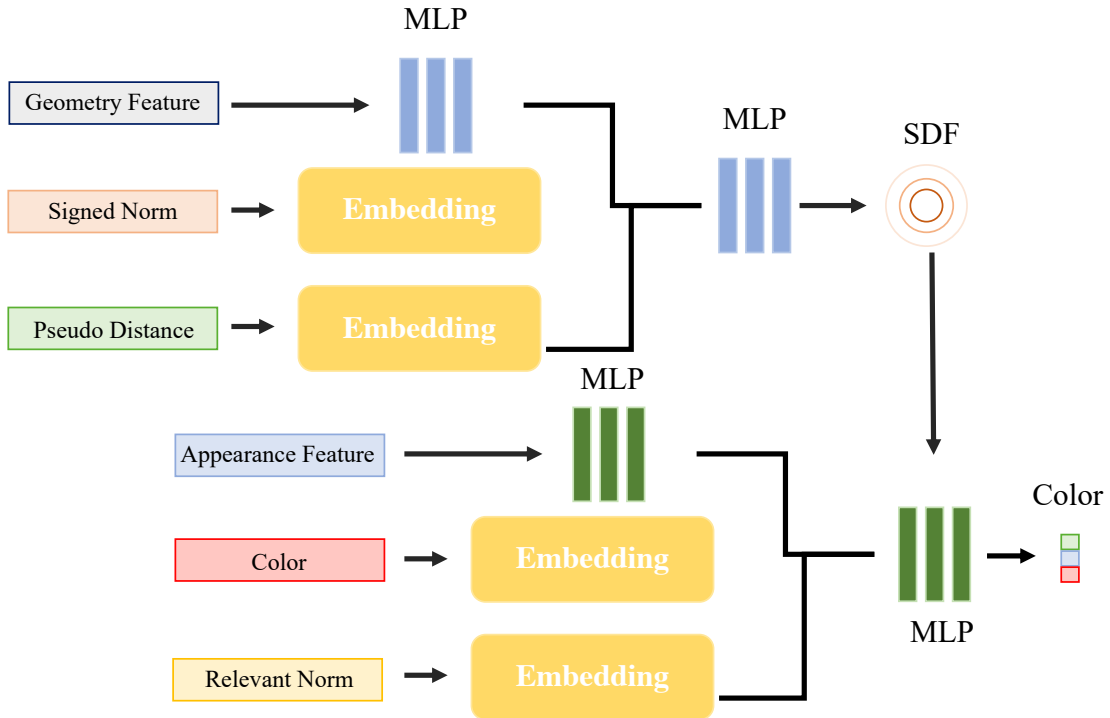
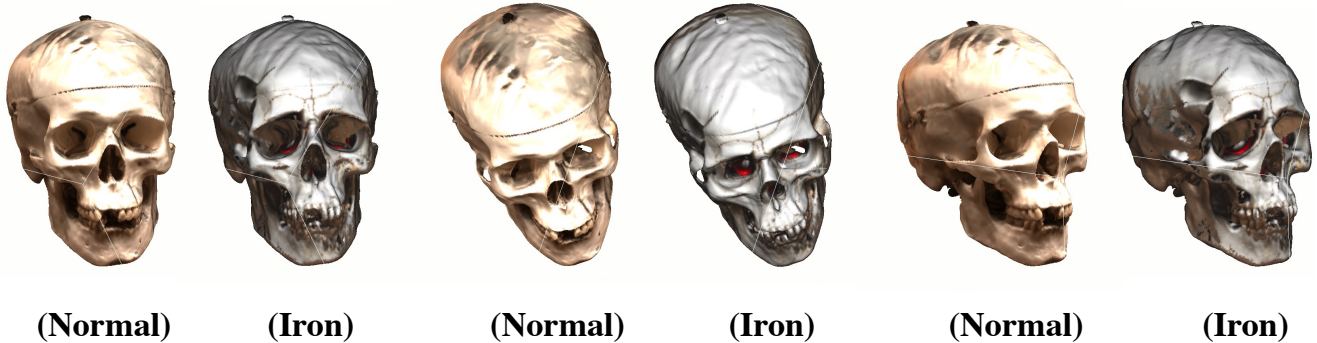


Figure 9. **Detailed Structure of Proposed SERF.** This figure illustrates the architecture of the MLPs employed in SERF. The term “Embedding” refers to the positional embedding introduced in the original NeRF [38].



**Figure 10. Texture Change With the Help Of Diffusion Model.** We introduced a method for texture modification through the utilization of the diffusion mode. This involves applying a diffusion model to alter the texture of the proposed model and subsequently employing the resulting image to construct a neural mesh.

where  $TP_i$  is the number of true positive pixels;  $FP_i$  is the number of false positive pixels;  $FN_i$  is the number of false negative pixels;  $N$  is the number of classes.

$$\text{Accuracy} = \frac{TP + TN}{TP + TN + FP + FN}; \quad (19)$$

where  $TN$  is the number of true negative pixels,

### 6.2.2 Interactive Segmentation

Thanks to our innovative interactive segmentation method, our approach is capable of producing consistent 3D mesh segmentation with just a single-point prompt (one point for the object and one for the rest). We present additional examples here to showcase the method’s performance as in Fig. 8. It is evident that our algorithm can yield plausible results for 3D mesh segmentation when guided by user-provided 3D instructions.

### 6.2.3 Geometry & Texture Editing

In addition to the suggested texture painting discussed in the main text, our approach also accommodates texture modification inspired by recent Diffusion works [48], as illustrated in Fig. 10. Here, we utilize a diffusion model to replace the original texture with an iron texture. The generated mesh from this process can be subsequently employed in the subsequent stages to achieve precise view synthesis.

## References

- [1] Kara-Ali Aliev, Artem Sevastopolsky, Maria Kolos, Dmitry Ulyanov, and Victor Lempitsky. Neural point-based graphics. 2020. 2
- [2] Jakob Andreas Bærentzen and Henrik Aanaes. Signed distance computation using the angle weighted pseudonormal. *IEEE Transactions on Visualization and Computer Graphics*, 11(3):243–253, 2005. 4
- [3] Chong Bao, Yinda Zhang, Bangbang Yang, Tianxing Fan, Zesong Yang, Hujun Bao, Guofeng Zhang, and Zhaopeng Cui. Sine: Semantic-driven image-based nerf editing with prior-guided editing field. In *Proceedings of the IEEE/CVF Conference on Computer Vision and Pattern Recognition*, pages 20919–20929, 2023. 1, 9
- [4] Jonathan T. Barron, Ben Mildenhall, Dor Verbin, Pratul P. Srinivasan, and Peter Hedman. Mip-nerf 360: Unbounded anti-aliased neural radiance fields. In *CVPR*, 2022. 1
- [5] Wang Bing, Lu Chen, and Bo Yang. Dm-nerf: 3d scene geometry decomposition and manipulation from 2d images. *arXiv preprint arXiv:2208.07227*, 2022. 2
- [6] Mathilde Caron, Hugo Touvron, Ishan Misra, Hervé Jégou, Julien Mairal, Piotr Bojanowski, and Armand Joulin. Emerging properties in self-supervised vision transformers. In *Proceedings of the International Conference on Computer Vision (ICCV)*, 2021. 3
- [7] Jiazhong Cen, Zanwei Zhou, Jiemin Fang, Wei Shen, Lingxi Xie, Xiaopeng Zhang, and Qi Tian. Segment anything in 3d with nerfs. *arXiv preprint arXiv:2304.12308*, 2023. 5, 8
- [8] Anpei Chen, Zexiang Xu, Fuqiang Zhao, Xiaoshuai Zhang, Fanbo Xiang, Jingyi Yu, and Hao Su. Mvsnerf: Fast generalizable radiance field reconstruction from multi-view stereo. In *Proceedings of the IEEE/CVF International Conference on Computer Vision*, pages 14124–14133, 2021. 1
- [9] Anpei Chen, Zexiang Xu, Andreas Geiger, Jingyi Yu, and Hao Su. Tensorf: Tensorial radiance fields. In *European Conference on Computer Vision (ECCV)*, 2022. 2
- [10] Yaosen Chen, Qi Yuan, Zhiqiang Li, Yuegen Liu, Wei Wang, Chaoping Xie, Xuming Wen, and Qien Yu. UPST-NeRF: Universal photorealistic style transfer of neural radiance fields for 3d scene. In *arXiv preprint arXiv:2208.07059*, 2022. 1
- [11] Pei-Ze Chiang, Meng-Shiun Tsai, Hung-Yu Tseng, Wei-Sheng Lai, and Wei-Chen Chiu. Styling 3d scene via implicit representation and hypernetwork. In *Proceedings of the IEEE/CVF Winter Conference on Applications of Computer Vision*, pages 1475–1484, 2022. 1
- [12] Chong Bao and Bangbang Yang, Zeng Junyi, Bao Hujun, Zhang Yinda, Cui Zhaopeng, and Zhang Guofeng. Neumesh: Learning disentangled neural mesh-based implicit field for geometry and texture editing. In *European Conference on Computer Vision (ECCV)*, 2022. 1, 3, 5, 7
- [13] Peng Dai, Yinda Zhang, Zhuwen Li, Shuaicheng Liu, and Bing Zeng. Neural point cloud rendering via multi-plane projection. In *Proceedings of the IEEE/CVF Conference on Computer Vision and Pattern Recognition*, pages 7830–7839, 2020. 2
- [14] Zhiwen Fan, Yifan Jiang, Peihao Wang, Xinyu Gong, Dejia Xu, and Zhangyang Wang. Unified implicit neural stylization. *arXiv preprint arXiv:2204.01943*, 2022. 1
- [15] Zhiwen Fan, Peihao Wang, Yifan Jiang, Xinyu Gong, Dejia Xu, and Zhangyang Wang. Nerf-sos: Any-view self-supervised object segmentation on complex scenes. *arXiv preprint arXiv:2209.08776*, 2022. 2
- [16] Xiao Fu, Shangzhan Zhang, Tianrun Chen, Yichong Lu, Lanyun Zhu, Xiaowei Zhou, Andreas Geiger, and Yiyi Liao. Panoptic nerf: 3d-to-2d label transfer for panoptic urban scene segmentation. In *3DV*, 2022. 2
- [17] Jun Gao, Tianchang Shen, Zian Wang, Wenzheng Chen, Kangxue Yin, Daiqing Li, Or Litany, Zan Gojcic, and Sanja Fidler. Get3d: A generative model of high quality 3d textured shapes learned from images. In *Advances In Neural Information Processing Systems*, 2022. 1
- [18] Rahul Goel, Dhawal Sirikonda, Saurabh Saini, and PJ Narayanan. Interactive segmentation of radiance fields. *arXiv preprint arXiv:2212.13545*, 2022. 2, 8
- [19] Michelle Guo, Alireza Fathi, Jiajun Wu, and Thomas Funkhouser. Object-centric neural scene rendering. *arXiv preprint arXiv:2012.08503*, 2020. 3
- [20] Jon Hasselgren, Nikolai Hofmann, and Jacob Munkberg. Shape, Light, and Material Decomposition from Images using Monte Carlo Rendering and Denoising. *arXiv:2206.03380*, 2022. 3
- [21] Benran Hu, Junkai Huang, Yichen Liu, Yu-Wing Tai, and Chi-Keung Tang. Instance neural radiance field. *arXiv preprint arXiv:2304.04395*, 2023. 2
- [22] Jinkai Hu, Chengzhong Yu, Hongli Liu, Lingqi Yan, Yiqian Wu, and Xiaogang Jin. Deep real-time volumetric rendering using multi-feature fusion. In *ACM SIGGRAPH 2023 Conference Proceedings*, New York, NY, USA, 2023. Association for Computing Machinery. 3
- [23] Yi-Hua Huang, Yue He, Yu-Jie Yuan, Yu-Kun Lai, and Lin Gao. Stylizednerf: consistent 3d scene stylization as stylized nerf via 2d-3d mutual learning. In *Proceedings of the IEEE/CVF Conference on Computer Vision and Pattern Recognition*, pages 18342–18352, 2022. 1
- [24] Rasmus Jensen, Anders Dahl, George Vogiatzis, Engin Tola, and Henrik Aanaes. Large scale multi-view stereopsis evaluation. In *Proceedings of the IEEE conference on computer vision and pattern recognition*, pages 406–413, 2014. 7
- [25] Justin Kerr, Chung Min Kim, Ken Goldberg, Angjoo Kanazawa, and Matthew Tancik. Lerf: Language embedded radiance fields. *arXiv preprint arXiv:2303.09553*, 2023. 2
- [26] Natasha Kholgade, Tomas Simon, Alexei Efros, and Yaser Sheikh. 3d object manipulation in a single photograph using stock 3d models. *ACM Transactions on Computer Graphics*, 33(4), 2014. 3
- [27] Sosuke Kobayashi, Eiichi Matsumoto, and Vincent Sitzmann. Decomposing nerf for editing via feature field distillation. In *NeurIPS*, 2022. 2
- [28] Zhengfei Kuang, Fujun Luan, Sai Bi, Zhixin Shu, Gordon Wetzstein, and Kalyan Sunkavalli. Palettenerf: Palette-based appearance editing of neural radiance fields. *arXiv preprint arXiv:2212.10699*, 2022. 3

- [29] Zhengqin Li, Mohammad Shafiei, Ravi Ramamoorthi, Kalyan Sunkavalli, and Manmohan Chandraker. Inverse rendering for complex indoor scenes: Shape, spatially-varying lighting and svbrdf from a single image. In *Proceedings of the IEEE/CVF Conference on Computer Vision and Pattern Recognition*, pages 2475–2484, 2020. 3
- [30] Zhengqi Li, Wenqi Xian, Abe Davis, and Noah Snavely. Crowdsampling the plenoptic function. In *European Conference on Computer Vision*, pages 178–196. Springer, 2020. 2
- [31] Zhengqin Li, Jia Shi, Sai Bi, Rui Zhu, Kalyan Sunkavalli, Miloš Hašan, Zexiang Xu, Ravi Ramamoorthi, and Manmohan Chandraker. Physically-based editing of indoor scene lighting from a single image. In *Computer Vision–ECCV 2022: 17th European Conference, Tel Aviv, Israel, October 23–27, 2022, Proceedings, Part VI*, pages 555–572. Springer, 2022. 3
- [32] Chen-Hsuan Lin, Wei-Chiu Ma, Antonio Torralba, and Simon Lucey. Barf: Bundle-adjusting neural radiance fields. In *IEEE International Conference on Computer Vision (ICCV)*, 2021. 2
- [33] Steven Liu, Xiuming Zhang, Zhoutong Zhang, Richard Zhang, Jun-Yan Zhu, and Bryan Russell. Editing conditional radiance fields. In *Proceedings of the International Conference on Computer Vision (ICCV)*, 2021. 3
- [34] Xinhang Liu, Jiaben Chen, Huai Yu, Yu-Wing Tai, and Chi-Keung Tang. Unsupervised multi-view object segmentation using radiance field propagation. In *NeurIPS*, 2022. 2
- [35] Stephen Lombardi, Tomas Simon, Jason Saragih, Gabriel Schwartz, Andreas Lehrmann, and Yaser Sheikh. Neural volumes: Learning dynamic renderable volumes from images. *ACM Trans. Graph.*, 38(4):65:1–65:14, 2019. 2
- [36] Ben Mildenhall, Pratul P. Srinivasan, Rodrigo Ortiz-Cayon, Nima Khademi Kalantari, Ravi Ramamoorthi, Ren Ng, and Abhishek Kar. Local light field fusion: Practical view synthesis with prescriptive sampling guidelines. *ACM Transactions on Graphics (TOG)*, 2019. 2
- [37] Ben Mildenhall, Pratul P. Srinivasan, Rodrigo Ortiz-Cayon, Nima Khademi Kalantari, Ravi Ramamoorthi, Ren Ng, and Abhishek Kar. Local light field fusion: Practical view synthesis with prescriptive sampling guidelines. *ACM Transactions on Graphics (TOG)*, 38(4):1–14, 2019. 7
- [38] Ben Mildenhall, Pratul P. Srinivasan, Matthew Tancik, Jonathan T. Barron, Ravi Ramamoorthi, and Ren Ng. Nerf: Representing scenes as neural radiance fields for view synthesis. In *ECCV*, 2020. 1, 4, 7, 11
- [39] Ben Mildenhall, Pratul P. Srinivasan, Matthew Tancik, Jonathan T. Barron, Ravi Ramamoorthi, and Ren Ng. Nerf: Representing scenes as neural radiance fields for view synthesis. In *ECCV*, 2020. 2
- [40] Thomas Müller, Alex Evans, Christoph Schied, and Alexander Keller. Instant neural graphics primitives with a multiresolution hash encoding. *ACM Trans. Graph.*, 41(4):102:1–102:15, 2022. 2
- [41] Jacob Munkberg, Jon Hasselgren, Tianchang Shen, Jun Gao, Wenzheng Chen, Alex Evans, Thomas Müller, and Sanja Fidler. Extracting triangular 3d models, materials, and lighting from images. In *Proceedings of the IEEE/CVF Conference on Computer Vision and Pattern Recognition*, pages 8280–8290, 2022. 3
- [42] Michael Niemeyer and Andreas Geiger. GIRAFFE: representing scenes as compositional generative neural feature fields. In *CVPR*, 2021. 2
- [43] Sida Peng, Yuanqing Zhang, Yinghao Xu, Qianqian Wang, Qing Shuai, Hujun Bao, and Xiaowei Zhou. Neural body: Implicit neural representations with structured latent codes for novel view synthesis of dynamic humans. In *CVPR*, 2021. 2
- [44] Patrick Pérez, Michel Gangnet, and Andrew Blake. Poisson image editing. In *ACM SIGGRAPH 2003 Papers*, pages 313–318. 2003. 3
- [45] René Ranftl, Alexey Bochkovskiy, and Vladlen Koltun. Vision transformers for dense prediction. *ArXiv preprint*, 2021. 3
- [46] Zhongzheng Ren, Aseem Agarwala, Bryan Russell, Alexander G Schwing, and Oliver Wang. Neural volumetric object selection. In *Proceedings of the IEEE/CVF Conference on Computer Vision and Pattern Recognition*, pages 6133–6142, 2022. 7
- [47] Zhongzheng Ren, Aseem Agarwala, Bryan C. Russell, Alexander G. Schwing, and Oliver Wang. Neural volumetric object selection. In *CVPR*, 2022. 2, 8
- [48] Robin Rombach, Andreas Blattmann, Dominik Lorenz, Patrick Esser, and Björn Ommer. High-resolution image synthesis with latent diffusion models. In *Proceedings of the IEEE/CVF conference on computer vision and pattern recognition*, pages 10684–10695, 2022. 12
- [49] Carsten Rother, Vladimir Kolmogorov, and Andrew Blake. “grabcut”: interactive foreground extraction using iterated graph cuts. *ACM Trans. Graph.*, 2004. 8
- [50] Sara Fridovich-Keil and Alex Yu, Matthew Tancik, Qinhong Chen, Benjamin Recht, and Angjoo Kanazawa. Plenoxels: Radiance fields without neural networks. In *CVPR*, 2022. 2
- [51] Rakshith Shetty, Mario Fritz, and Bernt Schiele. Adversarial scene editing: Automatic object removal from weak supervision. In *Advances in Neural Information Processing Systems 31*, pages 7716–7726, Montréal, Canada, 2018. Curran Associates. 3
- [52] Yawar Siddiqui, Lorenzo Porzi, Samuel Rota Bulò, Norman Müller, Matthias Nießner, Angela Dai, and Peter Kortschieder. Panoptic lifting for 3d scene understanding with neural fields. In *Proceedings of the IEEE/CVF Conference on Computer Vision and Pattern Recognition (CVPR)*, 2023. 2
- [53] Vincent Sitzmann, Justus Thies, Felix Heide, Matthias Nießner, Gordon Wetzstein, and Michael Zollhöfer. Deepvoxels: Learning persistent 3d feature embeddings. In *Proc. Computer Vision and Pattern Recognition (CVPR), IEEE*, 2019. 2
- [54] Vincent Sitzmann, Michael Zollhöfer, and Gordon Wetzstein. Scene representation networks: Continuous 3d-structure-aware neural scene representations. In *Advances in Neural Information Processing Systems*, 2019. 2

- [55] Karl Stelzner, Kristian Kersting, and Adam R Kosiorek. Decomposing 3d scenes into objects via unsupervised volume segmentation. *arXiv preprint arXiv:2104.01148*, 2021. 2
- [56] Cheng Sun, Min Sun, and Hwann-Tzong Chen. Direct voxel grid optimization: Super-fast convergence for radiance fields reconstruction. In *CVPR*, 2022. 2
- [57] Jiaxiang Tang, Xiaokang Chen, Jingbo Wang, and Gang Zeng. Compressible-composable nerf via rank-residual decomposition. *arXiv preprint arXiv:2205.14870*, 2022. 2
- [58] Vadim Tschernezki, Iro Laina, Diane Larlus, and Andrea Vedaldi. Neural feature fusion fields: 3d distillation of self-supervised 2d image representations. In *3DV*, 2022. 2
- [59] Suhani Vora, Noha Radwan, Klaus Greff, Henning Meyer, Kyle Genova, Mehdi SM Sajjadi, Etienne Pot, Andrea Tagliasacchi, and Daniel Duckworth. Nesf: Neural semantic fields for generalizable semantic segmentation of 3d scenes. *arXiv preprint arXiv:2111.13260*, 2021. 2
- [60] Peng Wang, Lingjie Liu, Yuan Liu, Christian Theobalt, Taku Komura, and Wenping Wang. Neus: Learning neural implicit surfaces by volume rendering for multi-view reconstruction. *arXiv preprint arXiv:2106.10689*, 2021. 2, 3, 5, 7, 9
- [61] Peng-Shuai Wang, Yang Liu, and Xin Tong. Dual octree graph networks for learning adaptive volumetric shape representations. *ACM Transactions on Graphics (TOG)*, 41(4):1–15, 2022. 4
- [62] Xiangyu Wang, Jingsen Zhu, Qi Ye, Yuchi Huo, Yunlong Ran, Zhihua Zhong, and Jiming Chen. Seal-3d: Interactive pixel-level editing for neural radiance fields. In *Proceedings of the IEEE/CVF International Conference on Computer Vision*, pages 17683–17693, 2023. 1
- [63] Chung-Yi Weng, Brian Curless, Pratul P. Srinivasan, Jonathan T. Barron, and Ira Kemelmacher-Shlizerman. HumanNeRF: Free-viewpoint rendering of moving people from monocular video. In *Proceedings of the IEEE/CVF Conference on Computer Vision and Pattern Recognition (CVPR)*, pages 16210–16220, 2022. 2
- [64] Fanbo Xiang, Zexiang Xu, Milos Hasan, Yannick Hold-Geoffroy, Kalyan Sunkavalli, and Hao Su. Neutex: Neural texture mapping for volumetric neural rendering. In *Proceedings of the IEEE/CVF Conference on Computer Vision and Pattern Recognition*, pages 7119–7128, 2021. 5, 7
- [65] Bangbang Yang, Yinda Zhang, Yinghao Xu, Yijin Li, Han Zhou, Hujun Bao, Guofeng Zhang, and Zhaopeng Cui. Learning object-compositional neural radiance field for editable scene rendering. In *International Conference on Computer Vision (ICCV)*, 2021. 3
- [66] Lior Yariv, Yoni Kasten, Dror Moran, Meirav Galun, Matan Atzmon, Basri Ronen, and Yaron Lipman. Multiview neural surface reconstruction by disentangling geometry and appearance. *Advances in Neural Information Processing Systems*, 33:2492–2502, 2020. 7
- [67] Lior Yariv, Jiatao Gu, Yoni Kasten, and Yaron Lipman. Volume rendering of neural implicit surfaces. In *Thirty-Fifth Conference on Neural Information Processing Systems*, 2021. 2
- [68] Weicai Ye, Shuo Chen, Chong Bao, Hujun Bao, Marc Pollefeys, Zhaopeng Cui, and Guofeng Zhang. Intrinsicnerf: Learning intrinsic neural radiance fields for editable novel view synthesis. 2022. 3
- [69] Hong-Xing Yu, Leonidas J. Guibas, and Jiajun Wu. Unsupervised discovery of object radiance fields. In *ICLR*, 2022. 2
- [70] Zehao Yu, Songyou Peng, Michael Niemeyer, Torsten Sattler, and Andreas Geiger. Monosdf: Exploring monocular geometric cues for neural implicit surface reconstruction. *Advances in Neural Information Processing Systems (NeurIPS)*, 2022. 2
- [71] Yu-Jie Yuan, Yang-Tian Sun, Yu-Kun Lai, Yuewen Ma, Rongfei Jia, and Lin Gao. Nerf-editing: geometry editing of neural radiance fields. In *Proceedings of the IEEE/CVF Conference on Computer Vision and Pattern Recognition*, pages 18353–18364, 2022. 1
- [72] Kai Zhang, Nick Kolkin, Sai Bi, Fujun Luan, Zexiang Xu, Eli Shechtman, and Noah Snavely. Arf: Artistic radiance fields. In *European Conference on Computer Vision*, pages 717–733. Springer, 2022. 1
- [73] Xiuming Zhang, Pratul P Srinivasan, Boyang Deng, Paul Debevec, William T Freeman, and Jonathan T Barron. Nerfactor: Neural factorization of shape and reflectance under an unknown illumination. *ACM Transactions on Graphics (TOG)*, 40(6):1–18, 2021. 3
- [74] Shuaifeng Zhi, Tristan Laidlow, Stefan Leutenegger, and Andrew J. Davison. In-place scene labelling and understanding with implicit scene representation. In *ICCV*, 2021. 2
- [75] Kaichen Zhou, Jia-Xing Zhong, Sangyun Shin, Kai Lu, Yiyuan Yang, Andrew Markham, and Niki Trigoni. Dynpoint: Dynamic neural point for view synthesis. *arXiv preprint arXiv:2310.18999*, 2023. 9
- [76] Tinghui Zhou, Richard Tucker, John Flynn, Graham Fyffe, and Noah Snavely. Stereo magnification: Learning view synthesis using multiplane images. In *SIGGRAPH*, 2018. 2
- [77] Jingsen Zhu, Fujun Luan, Yuchi Huo, Zihao Lin, Zhihua Zhong, Dianbing Xi, Rui Wang, Hujun Bao, Jiaxiang Zheng, and Rui Tang. Learning-based inverse rendering of complex indoor scenes with differentiable monte carlo raytracing. In *SIGGRAPH Asia 2022 Conference Papers*. ACM, 2022. 3
- [78] Jingsen Zhu, Yuchi Huo, Qi Ye, Fujun Luan, Jifan Li, Dianbing Xi, Lisha Wang, Rui Tang, Wei Hua, Hujun Bao, et al. I2-sdf: Intrinsic indoor scene reconstruction and editing via raytracing in neural sdbs. In *Proceedings of the IEEE/CVF Conference on Computer Vision and Pattern Recognition*, pages 12489–12498, 2023. 3